

Component based model order reduction with mortar tied contact for nonlinear quasi-static mechanical problems

Stephan Ritzert^{a,*}, Jannick Kehls^a, Stefanie Reese^{a,b}, Tim Brepols^a

^a*Institute of Applied Mechanics, RWTH Aachen University,*

Mies-van-der-Rohe-Str. 1, 52074 Aachen, Germany

^b*University of Siegen, 57076 Siegen, Germany*

{stephan.ritzert, jannick.kehls, stefanie.reese, tim.brepols}@ifam.rwth-aachen.de

Abstract. In this work, we present a model order reduction technique for nonlinear structures assembled from components. The reduced order model is constructed by reducing the substructures with proper orthogonal decomposition and connecting them by a mortar-tied contact formulation. The substructure projection matrices are computed by the proper orthogonal decomposition (POD) method from snapshots computed on the substructure level. The snapshots are computed using Latin hypercube sampling based on a parametrization of the boundary conditions. In numerical examples, we show the accuracy and efficiency of the method for nonlinear problems involving material and geometric nonlinearities as well as non-matching meshes. The method can predict solutions of new systems with varying boundary conditions and material behaviors.

Keywords: model-order reduction, nonlinear mechanics, substructuring, mortar method

1 Introduction

Many engineering structures are made of components. High-resolution finite element simulations of such systems are computationally expensive, especially for problems involving geometric and material nonlinearities. Model order reduction (MOR) can reduce this effort. In this work, we propose a method where the reduced order model (ROM) of a nonlinear modular system is constructed from ROMs of the substructures.

The coupling of reduced substructures has a long history for linear dynamical systems. For

an overview of the historical development of those methods, the reader is kindly referred to de Klerk et al. [2008]. A very popular component mode synthesis method is the Craig-Bampton method (Craig and Bampton [1968]), where the internal degrees of freedom (DOFs) are approximated by a combination of eigenmodes and so-called static constraint modes. The static constraint modes linearly relate the boundary DOFs to the internal DOFs and are computed by a static condensation of the stiffness matrix. Not many works exist that extend these component mode synthesis methods to nonlinear problems. For geometric nonlinearities, there exist works by Wenneker [2013], Kuether et al. [2016, 2017], and Bui et al. [2024] that extend the Craig-Bampton method (Craig and Bampton [1968]). In Kuether et al. [2016, 2017], a Craig-Bampton approximation of the displacement is used where the internal DOFs are reduced eigenmodes and static constraint modes. All of these quantities are computed from the linear stiffness matrix. Bui et al. [2024] enhanced the Craig-Bampton approach by static modal derivatives to account for the nonlinearity. In all of these works, the nonlinear force vector and stiffness matrix are approximated by cubic polynomial functions. This approximation is only valid for St. Venant-Kirchhoff materials and geometric nonlinearities. For large strains and nonlinear materials, the static constraint modes would also be a function of the displacement and would need to be updated in every Newton iteration. These methods only hold for small strains with large rotations because the static constraint modes are computed from the linear stiffness matrix.

In this work, we propose a data-driven reduction method where the DOFs of each substructure are reduced by the proper orthogonal decomposition (POD) method. The POD-Galerkin method (Lenaerts et al. [2001]) reduces the size of the system of equations and increases the speed of the solution of the solution. In the past it was successfully applied to solve nonlinear solid mechanics problems, see e.g. Lenaerts et al. [2001]; Herkt et al. [2009]; Radermacher and Reese [2013a,b]. An overview of POD in the field of structural dynamics is given in Kerschen et al. [2005]. A drawback of POD based model order reduction is that the solution time still depends on the original size of the problem, because in every iteration the nonlinear force vector and the tangential stiffness matrix have to be assembled. Therefore, different hyperreduction techniques were developed that can reduce the computational time to assemble the system. For recent works of POD based hyperreduction techniques in nonlinear mechanics, see among others: energy conserving sampling and weighting (Farhat et al. [2015]), discrete empirical interpolation method for nonlinear solid mechanics (Radermacher and Reese [2016]; Ghavamian et al. [2017]), (continuous) empirical cubature method (Hernández et al. [2017, 2024]), hyperreduction for nonlinear structural dynamics Rutzmoser [2018], hyperreduction for nonlinear computational homogenization problems (e.g. Guo et al. [2024]; Wulfinghoff [2024]). In this work, we present a POD-based component-wise MOR method, which is the foundation of future works including hyperreduction.

Not many works use POD-based MOR in substructuring problems, where the ROM of the whole system is assembled from the ROMs of the components. For linear problems component-wise

POD was used in Ritzert et al. [2023], where it was applied to parametric substructures and in McBane et al. [2022], where it was used for topology optimization of lattice-like structures. In nonlinear mechanics Zhou et al. [2018] proposed a method where the components are reduced by POD and connected by a penalty method. The penalty matrices are also reduced by parts of the substructure POD bases. In Hernández [2020] a method was proposed to compute periodic structures by another component-based MOR approach. In this approach, the substructures are coupled by fictitious interfaces.

In this work, we propose a new approach. We use a mortar-tied contact formulation as a basis and reduce the degrees of freedom of the substructures by individual pre-computed POD bases. The mortar method is a state-of-the-art contact mechanics method for non-matching meshes. An advantage of the method is, that the Lagrange multipliers, as well as the slave-side DOFs, can be removed from the equation system by static condensation, by choosing dual shape functions for the Lagrange multipliers. This property is used in this MOR technique. For more information regarding the mortar method for tied-contact, the reader is referred to e.g. Wohlmuth [2001]; Puso [2004]; Laursen et al. [2012]; Popp and Wriggers [2018]. Each substructure is reduced by POD projection matrices. The slave side interface DOFs are not reduced because they can be related to the reduced interface displacements of the master side.

In the numerical examples, we discuss the performance and accuracy of our method. We investigate large deformations, stability effects, different stiffnesses of the substructures, non-matching meshes and viscoelastic material behavior. For all numerical examples, the snapshots are computed on the substructure level. We parametrize the displacement boundary conditions and use a Latin hypercube sampling (LHS) procedure.

Outline of the paper In Section 2, we first discuss the mortar tied-contact full order model (Section 2.1) and then explain the component-based model order reduction technique, where the substructures are first reduced and then connected by the reduced mortar tied-contact (Section 2.2). The accuracy and performance of the MOR technique and the snapshot sampling are investigated in the numerical examples in Section 3. Finally, the results are discussed in Section 4.

2 Component based model order reduction

2.1 Full-order model

The full-order model (FOM) from which we derive our reduced-order model (ROM) is a mortar-tied-contact formulation with static condensation of the Lagrange multipliers and the contact

displacements on the slave side. In the following, it is briefly derived.

Weak formulation

In tied-contact problems, we introduce two conditions that must be fulfilled in addition to the balance of linear momentum. The first condition is that the displacements of two bodies must be equal on the contact interface $\Gamma_c^{1,2}$:

$$\mathbf{u}_c^1 = \mathbf{u}_c^2 \quad \text{on } \Gamma_c^{1,2} \quad (1)$$

The second condition is the equilibrium of the traction acting on the two bodies at the contact interface:

$$-\mathbf{t}_c^1 = \mathbf{t}_c^2 \quad \text{on } \Gamma_c^{1,2} \quad (2)$$

A tied-contact problem consisting of two substructures is displayed in Figure 1.

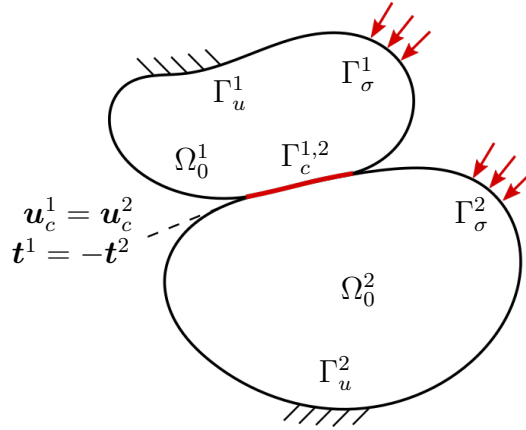


Figure 1: Illustration of a domain, that is composed of two subdomains Ω_0^1 and Ω_0^2 , with the Neumann boundaries Γ_σ^1 , and Γ_σ^2 and Dirichlet boundaries Γ_u^1 , and Γ_u^2 . At the contact interface $\Gamma_c^{1,2}$, the two tied contact conditions are displayed.

In this work, we use the Lagrange multiplier method to enforce those conditions. We introduce the Lagrange multiplier $\boldsymbol{\lambda} = -\mathbf{t}_c^1 = \mathbf{t}_c^2$ and come up with the variational saddle-point problem that can be derived from the Lagrange functional (see e.g. Wohlmuth [2001]):

$$\begin{aligned} \sum_{i=1}^{n_s} \delta g_{\text{int}}^i(\mathbf{u}, \delta \mathbf{u}) + \sum_{j=1}^{n_c} \delta g_{c,u}^j(\boldsymbol{\lambda}, \delta \mathbf{u}_c^1, \delta \mathbf{u}_c^2) &= 0 \\ \sum_{j=1}^{n_c} \delta g_{c,\lambda}^j(\mathbf{u}_c^1, \mathbf{u}_c^2, \delta \boldsymbol{\lambda}) &= 0 \end{aligned} \quad (3)$$

Here n_s is the number of substructures and n_c is the number of tied-contact interfaces. The displacements at the tied contact interfaces denoted by $\mathbf{u}_c^1, \mathbf{u}_c^2$ are subsets of the displacements

of the respective substructures that share that interface. The weak form of the balance of linear momentum for the quasi-static case is

$$\delta g_{\text{int}}^i = \int_{\Omega_0} (\mathbf{S} : \delta \mathbf{E} - \rho \mathbf{b} \cdot \delta \mathbf{u}) \, dV - \int_{\Gamma_t} \delta \mathbf{u} \cdot \mathbf{t} \, dA, \quad (4)$$

where \mathbf{S} is the second Piola-Kirchhoff stress tensor, $\delta \mathbf{E}$ is the virtual Green-Lagrange strain tensor, \mathbf{b} are the body forces, ρ is the density and \mathbf{t} are the tractions acting on the boundary Γ_t . From the variational Lagrange multiplier method, we get the following contributions that enforce the tied-contact constraints

$$\delta g_{c,u}^j = \int_{\Gamma_c^{1,2}} (\delta \mathbf{u}_c^1 - \delta \mathbf{u}_c^2) \cdot \boldsymbol{\lambda} \, dA \quad (5)$$

$$\delta g_{c,\lambda}^j = \int_{\Gamma_c^{1,2}} \delta \boldsymbol{\lambda} \cdot (\mathbf{u}_c^1 - \mathbf{u}_c^2) \, dA \quad (6)$$

Discretization

To solve Equation (3), we discretize Equation (4) to Equation (6) with the finite element method (FEM). A displacement-based discretization of Equation (4) leads to the nonlinear $n \times 1$ -dimensional vector equation

$$\mathbf{G}(\mathbf{U}(t), t) = \mathbf{R}(\mathbf{U}(t)) - \mathbf{F}_{\text{ext}}(t). \quad (7)$$

$\mathbf{R}(\mathbf{U}(t))$ is the internal force vector, that depends nonlinearly on the displacement vector $\mathbf{R}(\mathbf{U}(t))$ at time t , and $\mathbf{F}_{\text{ext}}(t)$ is the external force vector. The discretization of Equation (5) and Equation (6) yields

$$\delta g_{c,u} = \delta(\mathbf{U}_c^1)^T \mathbf{D}^T \boldsymbol{\Lambda} - \delta(\mathbf{U}_c^2)^T \mathbf{M}^T \boldsymbol{\Lambda} \quad (8)$$

$$\delta g_{c,\lambda} = \delta \boldsymbol{\Lambda}^T \mathbf{D} \mathbf{U}_c^1 - \delta \boldsymbol{\Lambda}^T \mathbf{M} \mathbf{U}_c^2 \quad (9)$$

where we introduce the mortar-matrices \mathbf{D} and \mathbf{M} . These matrices arise from a finite element discretization of the interface displacements $\mathbf{u}_c^i = \mathbf{N}^i \mathbf{U}_c^i$ and the Lagrange multipliers $\boldsymbol{\lambda} = \hat{\mathbf{N}}^1 \boldsymbol{\Lambda}$. \mathbf{N}^1 and \mathbf{N}^2 are shape functions for the displacements and the coordinates of the slave and master side interface elements. $\hat{\mathbf{N}}^1$ are the shape functions of the Lagrange multiplier, defined on the slave side of the interface. The mortar matrices are computed for all n_e interface elements and assembled into the matrices \mathbf{D} , \mathbf{M} . They are defined as:

$$\mathbf{D} = \mathbf{\hat{A}}_{e=1}^{n_e} \mathbf{D}^e, \quad \mathbf{D}^e = \int_{\Gamma_e^1} (\hat{\mathbf{N}}^1)^T \mathbf{N}^1 \, dA \quad (10)$$

$$\mathbf{M} = \mathbf{\hat{A}}_{e=1}^{n_e} \mathbf{M}^e, \quad \mathbf{M}^e = \int_{\Gamma_e^1} (\hat{\mathbf{N}}^1)^T \mathbf{N}^2 \, dA. \quad (11)$$

Here, \mathbf{A} is the assembly operator. The integrals on the element level can be solved by the mortar method (e.g. Puso [2004]; Popp and Wriggers [2018]). The advantage of this method is, that the integrals can be solved for non-conforming meshes.

The discretized equations for a system consisting of n_s substructures and n_c tied-contact interfaces reads

$$\sum_{i=1}^{n_s} \mathbf{G}_i(t, \mathbf{U}_i) + \sum_{j=1}^{n_c} (\mathbf{D}_j^T \boldsymbol{\Lambda}_j - \mathbf{M}_j^T \boldsymbol{\Lambda}_j) = 0 \quad (12)$$

$$\sum_{j=1}^{n_c} (\mathbf{D}_j \mathbf{U}_{c,j}^1 - \mathbf{M}_j \mathbf{U}_{c,j}^2) = 0 \quad (13)$$

Note, that the displacements of each contact interface j : $\mathbf{U}_{c,j}^1$ and $\mathbf{U}_{c,j}^2$ are a subset of the displacements of a substructure \mathbf{U}_i . Since $\mathbf{G}_i(t, \mathbf{U}_i)$ is a nonlinear vector, the above system of equations (Equations (12) and (13)) will be solved by the Newton-Raphson scheme. For the linearization of Equation (12) we define the tangential stiffness matrix of a substructure i for the displacement state \mathbf{U}_i^k as $\mathbf{K}_i(\mathbf{U}_i^k) := \frac{\partial \mathbf{G}_i}{\partial \mathbf{U}_i} |_{\mathbf{U}_i^k}$. To compute the solution of the $k+1$ iteration we solve the following equation system for all $\Delta \mathbf{U}_i$

$$\sum_{i=1}^{n_s} (\mathbf{G}_i(t, \mathbf{U}_i^k) + \mathbf{K}_i(\mathbf{U}_i^k) \Delta \mathbf{U}_i) + \sum_{j=1}^{n_c} (\mathbf{D}_j^T \boldsymbol{\Lambda}_j^k - \mathbf{M}_j^T \boldsymbol{\Lambda}_j^k) = 0 \quad (14)$$

$$\sum_{j=1}^{n_c} (\mathbf{D}_j \Delta \mathbf{U}_{c,j}^1 - \mathbf{M}_j \Delta \mathbf{U}_{c,j}^2) = 0 \quad (15)$$

The displacements of all substructures are then updated by $\mathbf{U}_i^{k+1} = \mathbf{U}_i^k + \Delta \mathbf{U}_i$. This procedure is repeated until Equations (12) and (13) are approximately fulfilled.

For simplicity, further derivations are shown for a system with two substructures, where one body is called master and the other is called slave. From now on, the master degrees of freedom will be denoted by a superscript M and the slave degrees of freedom by a superscript S . The displacements and residual vectors of each substructure are split into internal degrees of freedom \mathbf{U}_I , \mathbf{G}_I and tied contact degrees of freedom \mathbf{U}_C , \mathbf{G}_C . The tangential stiffness matrices are split accordingly into four block matrices. For this special case, Equations (14) and (15) can be written in matrix-vector notation:

$$\begin{bmatrix} \mathbf{K}_{II}^M & \mathbf{0} & \mathbf{K}_{IC}^M & \mathbf{0} & \mathbf{0} \\ \mathbf{0} & \mathbf{K}_{II}^S & \mathbf{0} & \mathbf{K}_{IC}^S & \mathbf{0} \\ \mathbf{K}_{CI}^M & \mathbf{0} & \mathbf{K}_{CC}^M & \mathbf{0} & -\mathbf{M}^T \\ \mathbf{0} & \mathbf{K}_{CI}^S & \mathbf{0} & \mathbf{K}_{CC}^S & \mathbf{D}^T \\ \mathbf{0} & \mathbf{0} & -\mathbf{M} & \mathbf{D} & \mathbf{0} \end{bmatrix} \begin{bmatrix} \Delta \mathbf{U}_I^M \\ \Delta \mathbf{U}_I^S \\ \Delta \mathbf{U}_C^M \\ \Delta \mathbf{U}_C^S \\ \boldsymbol{\Lambda} \end{bmatrix} = - \begin{bmatrix} \mathbf{G}_I^M \\ \mathbf{G}_I^S \\ \mathbf{G}_C^M \\ \mathbf{G}_C^S \\ \mathbf{0} \end{bmatrix} \quad (16)$$

This equation system has the typical saddle point structure with a zero block matrix on the main diagonal. It can have both positive and negative eigenvalues and is therefore indefinite (cf. e.g.

Rusten and Winther [1992]). The saddle point structure is unfavorable for efficient solution algorithms. It requires special preconditioning techniques to apply iterative solution methods like the conjugate gradient (CG), or the generalized minimal residual (GMRES) method (Saad [2003]; Benzi et al. [2005]). Moreover, the additional degrees of freedom would require additional mode matrices for the ROM. In this paper, we use the mortar method to compute the matrices \mathbf{D} and \mathbf{M} (Wohlmuth [2001]; Laursen et al. [2012]; Popp and Wriggers [2018]). The advantage of this method is, that the Lagrange multipliers can be removed from the system of equations in Equation (16), and it can be transformed into a symmetric positive definite system of equations. Another advantage is the integration procedure to compute the mortar matrices \mathbf{D} and \mathbf{M} , which allows for non-conforming meshes. The integration procedure is explained in detail in e.g. Puso [2004]; Popp and Wriggers [2018].

Static condensation

In this section, we describe how the system of equations in Equation (16) can be transformed into a symmetric positive definite system by static condensation. From the fifth equation in Equation (16), it follows that:

$$\Delta \mathbf{U}_C^S = \mathbf{D}^{-1} \mathbf{M} \Delta \mathbf{U}_C^M := \mathbf{P} \Delta \mathbf{U}_C^M \quad (17)$$

where $\mathbf{P} := \mathbf{D}^{-1} \mathbf{M}$ is the discrete interface coupling operator (Popp and Wriggers [2018]). The Lagrange multipliers $\mathbf{\Lambda}$ can be expressed as

$$\mathbf{\Lambda} = \mathbf{D}^{-T} (-\mathbf{g}_c^S - \mathbf{K}_{CI}^S \Delta \mathbf{U}_I^S - \mathbf{K}_{CC}^S \Delta \mathbf{U}_C^S) \quad (18)$$

by reordering the fourth equation of the equation system given in Equation (16). By inserting Equation (18) into the second and third equation of Equation (16) and utilizing Equation (17) we obtain the final condensed system of equations:

$$\underbrace{\begin{bmatrix} \mathbf{K}_{II}^M & \mathbf{0} & \mathbf{K}_{IC}^M \\ \mathbf{0} & \mathbf{K}_{II}^S & \mathbf{K}_{IC}^S \mathbf{P} \\ \mathbf{K}_{CI}^M & \mathbf{P}^T \mathbf{K}_{CI}^S & \mathbf{K}_{CC}^M + \mathbf{P}^T \mathbf{K}_{CC}^S \mathbf{P} \end{bmatrix}}_{\mathbf{K}_{\text{cond}}} \underbrace{\begin{bmatrix} \Delta \mathbf{U}_I^M \\ \Delta \mathbf{U}_I^S \\ \Delta \mathbf{U}_C^M \end{bmatrix}}_{\Delta \mathbf{U}_{\text{cond}}} = - \underbrace{\begin{bmatrix} \mathbf{G}_I^M \\ \mathbf{G}_I^S \\ \mathbf{G}_C^M + \mathbf{P}^T \mathbf{G}_C^S \end{bmatrix}}_{\mathbf{G}_{\text{cond}}} \quad (19)$$

Here also the definition of the interface coupling operator $\mathbf{P} := \mathbf{D}^{-1} \mathbf{M}$ is used. This static condensation requires the inversion of the mortar matrix \mathbf{D} , which for standard shape functions is computationally expensive. A solution to this problem was proposed by Wohlmuth [2001] by choosing dual shape functions for the Lagrange multipliers. Because of these dual shape functions, the mortar matrix \mathbf{D} reduces to a diagonal matrix that can be easily inverted.

The dual Lagrange multiplier shape functions \hat{N}_j^S are defined by the biorthogonality condition with the displacement shape functions N_k^S :

$$\int_{\Gamma_e} \hat{N}_j^S N_k^S dA = \delta_{jk} \int_{\Gamma_e} N_k^S dA \quad (20)$$

which was first presented in the works of Scott and Zhang [1990] and applied to the mortar method in Wohlmuth [2001]. The Lagrange multiplier shape functions are computed by a linear mapping of the standard displacement shape functions

$$\hat{N}_j^S = a_{jk} N_k^S \quad (21)$$

with the coefficient matrix $\mathbf{A} = [a_{jk}]$. The coefficients are obtained by the expression

$$\mathbf{A} = \mathbf{B}\mathbf{C}^{-1}, \quad (22)$$

stemming from the biorthogonality condition Equation (20). The entries of the matrices $\mathbf{B} = [b_{jk}]$ and $\mathbf{C} = [c_{jk}]$ are computed by

$$b_{jk} = \delta_{jk} \int_{\Gamma_e} N_k \, dA \quad (23)$$

$$c_{jk} = \int_{\Gamma_e} N_j N_k \, dA. \quad (24)$$

With the method described above, the condensed system of equations can be efficiently computed. It should be noted, that the interface-coupling operator \mathbf{P} only needs to be computed in the beginning. Only the residual vectors and tangential stiffness matrices of the substructures have to be evaluated in every iteration step. The condensed system of equations Equation (19) is the basis of the reduced-order model described in the following section.

2.2 Reduced-order model

Component based model order reduction

The idea of this model order reduction (MOR) technique is to reduce the DOFs of the substructures on their own and assemble them into a global reduced system of equations. The difference to the MOR techniques in Zhou et al. [2018]; Ritzert et al. [2023] is that we here use the mortar method for mesh-tying (cf. Section 2.1) instead of the penalty approach.

For the derivation of the ROM, we use a system composed of two substructures denoted by the superscripts S for the slave side and M for the master side (cf. Equation (16) to Equation (19)). The displacement vectors of the substructures are split into internal displacements $\mathbf{U}_I^{S,M}$ with $n_I^{S,M}$ degrees of freedom and interface displacements $\mathbf{U}_C^{S,M}$ with $n_C^{S,M}$ degrees of freedom. The displacements of the master side are approximated by the product

$$\mathbf{U}^M = \begin{bmatrix} \mathbf{U}_I^M \\ \mathbf{U}_C^M \end{bmatrix} \approx \begin{bmatrix} \mathbf{\Psi}_I^M \\ \mathbf{\Psi}_C^M \end{bmatrix} \mathbf{a}^M = \mathbf{\Psi}^M \mathbf{a}^M \quad (25)$$

where Ψ_I^M and Ψ_C^M are the internal and contact parts of the master-side projection matrix Ψ^M with the dimensions $n^M \times m^M$. The vector \mathbf{a}^M contains the m^M reduced displacements of the master substructure. The product

$$\mathbf{U}^S = \begin{bmatrix} \mathbf{U}_I^S \\ \mathbf{U}_C^S \end{bmatrix} \approx \begin{bmatrix} \Psi_I^S & \mathbf{0} \\ \mathbf{0} & \mathbf{I} \end{bmatrix} \begin{bmatrix} \mathbf{a}_I^S \\ \mathbf{U}_C^S \end{bmatrix} \quad (26)$$

approximates the slave-side displacements. Here, only the internal DOFs are approximated by the $n_I^S \times m_I^S$ -dimensional projection matrix Ψ_I^S and the corresponding unknowns \mathbf{a}_I^S . The slave-side interface displacements \mathbf{U}_C^S are not approximated since they can be expressed in terms of the interface-coupling operator \mathbf{P} and the approximation of the master-side displacements \mathbf{U}_C^M (cf. Equation (17))

$$\mathbf{U}_C^S = \mathbf{P} \Psi_C^M \mathbf{a}^M \quad (27)$$

The reduced system of equations is obtained by inserting the relations Equation (25), Equation (26) and Equation (27) into the condensed equation system Equation (19) and applying a Galerkin projection with the projection matrices Ψ_I^M , Ψ_I^S and Ψ_C^M . In the Galerkin projection we multiply the transposed projection matrices from the left side to the corresponding degrees of freedom. This leads to the reduced quantities:

$$\hat{\mathbf{K}}_{\text{cond}} = \begin{bmatrix} (\Psi^M)^T \mathbf{K}^M \Psi^M + (\Psi_c^M)^T \mathbf{P}^T \mathbf{K}_{cc}^S \mathbf{P} \Psi_c^M & (\Psi_c^M)^T \mathbf{P}^T \mathbf{K}_{ci}^S \Psi_i^S \\ (\Psi_i^M)^T \mathbf{K}_{ic}^S \mathbf{P} \Psi_c^M & (\Psi_i^S)^T \mathbf{K}_{ii}^S \Psi_i^S \end{bmatrix} \quad (28)$$

$$\Delta \mathbf{a}_{\text{cond}} = \begin{bmatrix} \Delta \mathbf{a}^M \\ \Delta \mathbf{a}_i^S \end{bmatrix} \quad (29)$$

$$\hat{\mathbf{G}}_{\text{cond}} = \begin{bmatrix} (\Psi^M)^T \mathbf{G}^M + (\Psi_c^M)^T \mathbf{P}^T \mathbf{G}_c^S \\ (\Psi_i^S)^T \mathbf{G}_i^S \end{bmatrix} \quad (30)$$

In Equation (28) the master-side contact and internal contributions are summed up:

$$\begin{aligned} (\Psi^M)^T \mathbf{K}^M \Psi^M &= (\Psi_i^M)^T \mathbf{K}_{ii}^M \Psi_i^M + (\Psi_i^M)^T \mathbf{K}_{ic}^M \Psi_c^M \\ &\quad + (\Psi_c^M)^T \mathbf{K}_{ci}^M \Psi_i^M + (\Psi_c^M)^T \mathbf{K}_{cc}^M \Psi_c^M \end{aligned} \quad (31)$$

$$(\Psi^M)^T \mathbf{G}^M = (\Psi_i^M)^T \mathbf{G}_i^M + (\Psi_c^M)^T \mathbf{G}_c^M \quad (32)$$

The Lagrange Multipliers can be computed from the reduced displacements by

$$\Lambda = \mathbf{D}^{-T} \left(-\mathbf{G}_C^S - \mathbf{K}_{CI}^S \Psi_I^S \Delta \mathbf{a}_I^S - \mathbf{K}_{CC}^S \mathbf{P} \Psi_C^M \Delta \mathbf{a}^M \right). \quad (33)$$

The discrete nonlinear system of reduced equations is solved by the Newton-Raphson method. The iterative solution algorithm for a time step is shown in Algorithm 1

Comment It should be noted, that for every iteration the residuals \mathbf{G}_S , \mathbf{G}_M and the tangential stiffness matrices \mathbf{K}_S , \mathbf{K}_M have to be computed for every substructure. The computational

Algorithm 1: Newton-Raphson solution of the nonlinear modular system

```

while  $\|\hat{\mathbf{G}}_{\text{cond}}(\mathbf{U}_j^M, \mathbf{U}_j^S)\| > \text{tol.}$  do
     $\Delta \mathbf{a} = - \left( \hat{\mathbf{K}}_{\text{cond}}(\mathbf{U}_j^M, \mathbf{U}_j^S) \right)^{-1} \hat{\mathbf{G}}_{\text{cond}}(\mathbf{U}_j^M, \mathbf{U}_j^S)$ 
     $\mathbf{U}_{j+1}^M = \mathbf{U}_j^M + \begin{bmatrix} \Psi_I^M \Delta \mathbf{a}^M \\ \Psi_C^M \Delta \mathbf{a}^M \end{bmatrix}$ 
     $\mathbf{U}_{j+1}^S = \mathbf{U}_j^S + \begin{bmatrix} \Psi_I^S \Delta \mathbf{a}_I^S \\ \mathbf{P} \Psi_C^M \Delta \mathbf{a}^M \end{bmatrix}$ 
     $j \leftarrow j + 1$ 
  
```

effort to solve the system is reduced but the computation of those matrices still depends on the original problem size $n = n_M + n_S$. At this stage hyperreduction techniques could be used to reduce this effort even further. In nonlinear solid mechanics the discrete empirical interpolation method (DEIM) (see Chaturantabut and Sorensen [2010]; Radermacher and Reese [2016]), (continuous) empirical cubature (Hernández et al. [2017, 2024]), or energy conserving sampling and weighting (ECSW) (Farhat et al. [2015]; Rutzmoser [2018]) proved to be well suited. However, having a working POD-based model order reduction is a necessary step towards hyperreduced component-based model order reduction. The extension to hyperreduction is out of the scope of this paper but will be addressed in future works.

Proper orthogonal decomposition

In the previous paragraph, we introduced the projection matrices Ψ_I^M , Ψ_C^M , and Ψ_I^S but have not mentioned yet how they can be computed. We use the proper orthogonal decomposition (POD) method to compute the projection matrices since it showed good results for nonlinear mechanics simulations (Radermacher and Reese [2013b]; Rutzmoser [2018]). In POD, the projection matrix is computed from collected data of l displacement states of the substructure, the so-called snapshots. The snapshots are stored in a matrix

$$\mathbf{S}_{\text{Snap}} = [\mathbf{U}_1, \mathbf{U}_2, \dots, \mathbf{U}_l] = \mathbf{\Phi} \mathbf{\Theta} \mathbf{\Omega} \quad (\text{SVD}) \quad (34)$$

which can be decomposed by a singular value decomposition (SVD) into the left and right mode matrix $\mathbf{\Phi}$ and $\mathbf{\Omega}$, respectively, as well as the singular values $\mathbf{\Theta}$. The projection matrix is constructed by selecting only the first m columns of $\mathbf{\Phi}$. Leading to the $n^s \times m$ dimensional projection matrix

$$\mathbf{\Psi} = [\mathbf{\Phi}_1, \dots, \mathbf{\Phi}_m], \quad (35)$$

where n^s is the number of DOFs of the substructure. The projection matrices for the internal DOFs Ψ_I^M and Ψ_I^S or interface DOFs Ψ_C^M are obtained by selecting the corresponding DOFs of the projection matrix of a substructure.

2.3 Computation of snapshots

For the component-wise model order reduction technique described in Section 2.2 suitable substructure modes are needed. These modes should give accurate results when the substructure is used in arbitrary structures and subjected to varying loading or tied-contact conditions. To compute such modes the snapshots should contain many deformation states that could possibly occur, such that the modes can be used in different structures under different loading conditions. To achieve this, we parametrize the boundary conditions applied on the possible interface surfaces of the substructures. The snapshots are computed by evaluating the full-order model of the substructure for different sample points in the parameter space. In this work, the sampling points are selected by the Latin hypercube sampling method (LHS), which creates sample points over the whole parameter space and avoids clustering. Other possible methods are greedy search methods, where the sample parameters are selected adaptively (see e.g. Bui-Thanh et al. [2008] or Haasdonk and Ohlberger [2008]). An overview of parametric model order reduction is given in Benner et al. [2015].

3 Numerical Examples

3.1 Example 1

3.1.1 Boundary value problem

In this numerical example, we use the same substructure in two different systems. For both systems, we use the same mode matrices, that we computed from the snapshots generated by the Latin hypercube sampling (cf. Section 2.3). This example demonstrates that the substructure modes can be used to predict solutions of systems under various loading conditions.

The first system consists of 6 substructures and is displayed in Figure 2. The substructure in the bottom right corner has a finer mesh than the other substructures. In total, the system has 29358 DOFs. Each substructure is characterized by a Neo-Hookean material behavior with a Young's modulus of $E = 80 \text{ GPa}$ and a Poisson's ratio of $\nu = 0.15$. In addition to this nonlinear material behavior, we also consider geometric nonlinearities by employing finite strain theory. Boundary conditions and dimensions are provided in Figure 2. The maximum displacement applied to the system is $\bar{u}_x^{\max} = 30 \text{ mm}$.

The second system consists of 9 substructures and is displayed in Figure 3. Here, all substructures have the same mesh, but the substructures marked in blue have a higher stiffness than the gray substructures. The blue substructures have a Young's modulus of $E = 80 \text{ GPa}$, the gray substructures of $E = 20 \text{ GPa}$, and all substructures have the same Poisson's ratio $\nu = 0.15$.

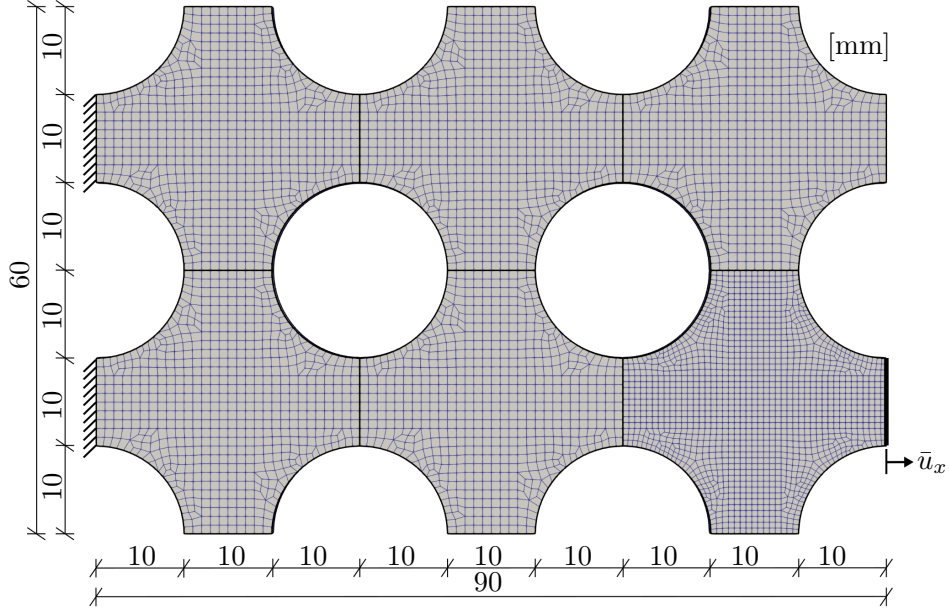


Figure 2: Geometry, mesh and boundary conditions of the 2×3 example. The substructure on the bottom right has a finer mesh than the other substructures.

The system has in total 36990 DOFs. The boundary conditions and dimensions can be taken from Figure 3. We apply a displacement in y -direction on the whole right surface, while fixing the x -displacement on that side.

3.1.2 Snapshot computation

Snapshots are computed at the substructure level using a Latin hypercube sampling procedure, as described in Section 2.3. The following parametrization is a specific choice, that aims to provide general snapshots that can be used to reduce arbitrary systems under varying loading conditions. Alternative parametrizations are possible and may lead to improved results.

We parametrize the Dirichlet boundary conditions on the four edges with in total ten parameters. Two parameters d_x , d_y for the normal displacements on the four edges. The x -displacement on the left and right edge depend on the parameter d_x . The y -displacement on the top and bottom edge is parametrized by d_y . Additionally, we prescribe perpendicular displacement and rotations of all four edges. The perpendicular displacements are described by the parameters p_y^l and p_y^r for the y -displacement on the left and right edge and p_x^t and p_x^b for the x -displacement at the top and bottom. The rotations of the edges lead to x - and y -displacements and are parametrized by the angles φ_z^l , φ_z^r , φ_z^t , φ_z^b . A snapshot is computed by applying a displacement vector at specific parameter point to a displacement driven nonlinear full-order simulation of the sub-

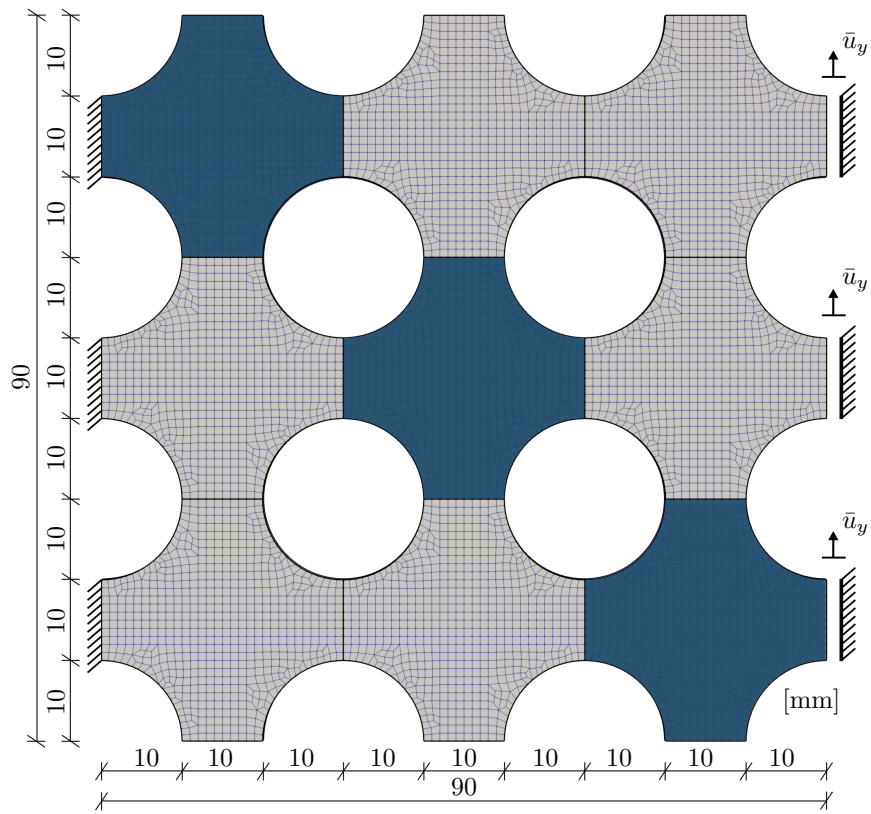


Figure 3: Geometry, mesh and boundary conditions of the 3×3 example. The blue substructures have a Young's modulus of $E = 80$ GPa, the gray substructures of $E = 20$ GPa.

structure. The snapshot parametrization is illustrated in Figure 4.

Prescribing these displacements to the x - and y -displacements of all four edges would lead to planar surfaces without strains. To circumvent this problem, we compute three different snapshots with different boundary conditions for every sample point. In the first case, we prescribe x - and y -displacements at all DOFs of all edges. In the second case, we prescribe only the normal displacements of each boundary, neglecting the displacement BCs stemming from the perpendicular parameters. Every node at the edges can freely deform in perpendicular direction. In the third case we prescribe only the perpendicular displacements and let the normal displacements remain unrestricted.

The parameter space used in the LHS is defined by:

$$\begin{aligned} d_x &\in (-1, 3) \text{ [mm]} & d_y &\in (-1, 3) \text{ [mm]} \\ p_x^l &\in (-3, 3) \text{ [mm]} & \varphi_z^l &\in (-15, 15) \text{ [}^\circ\text{]} \\ p_x^r &\in (-3, 3) \text{ [mm]} & \varphi_z^r &\in (-15, 15) \text{ [}^\circ\text{]} \\ p_y^t &\in (-3, 3) \text{ [mm]} & \varphi_z^t &\in (-15, 15) \text{ [}^\circ\text{]} \\ p_y^b &\in (-3, 3) \text{ [mm]} & \varphi_z^b &\in (-15, 15) \text{ [}^\circ\text{]} \end{aligned}$$

In this 10 dimensional parameter space we compute 50 sample points by LHS. At every sample points we compute two load steps for the three BC-cases described above, leading in the end to a total of 300 snapshots.

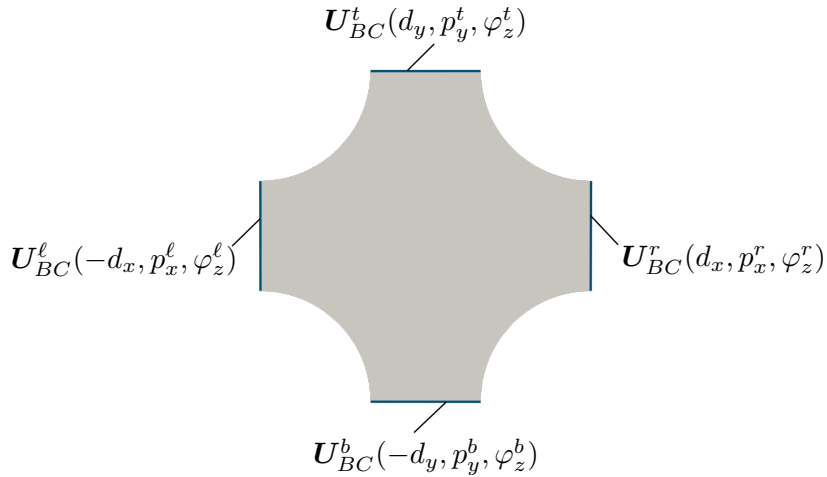


Figure 4: Illustration of the snapshot parametrization.

The POD modes are computed by the singular value decomposition of the snapshot matrix consisting of the snapshots from the LHS and three snapshots containing the rigid body translations and rotations. The decay of the normalized singular values is shown in Figure 5 on the left side. To assess the quality of the POD basis, we compute ten unseen test samples with increasing number of modes and analyze the mean displacement error e . The displacement error e is given

by

$$e = \frac{\|U_{\text{MOR}} - U_{\text{Ref}}\|}{\|U_{\text{Ref}}\|}, \quad (36)$$

where $\|\bullet\|$ denotes the L_2 norm of \bullet . The results can be seen on the right side of Figure 5. We show the mean values of the three boundary condition sets described above and the mean of all simulations. The blue area is the area between the minimum and maximum error. It can be seen, that the mean displacement error drops from $e = 21.6\%$ at 14 modes to $e = 3.7\%$ for 15 modes. Utilizing more modes does not reduce the error significantly. The mean error converges to a value of $e = 1.3\%$. The singular values show a similar behavior, where the slope of the decay decreases after 15 modes.

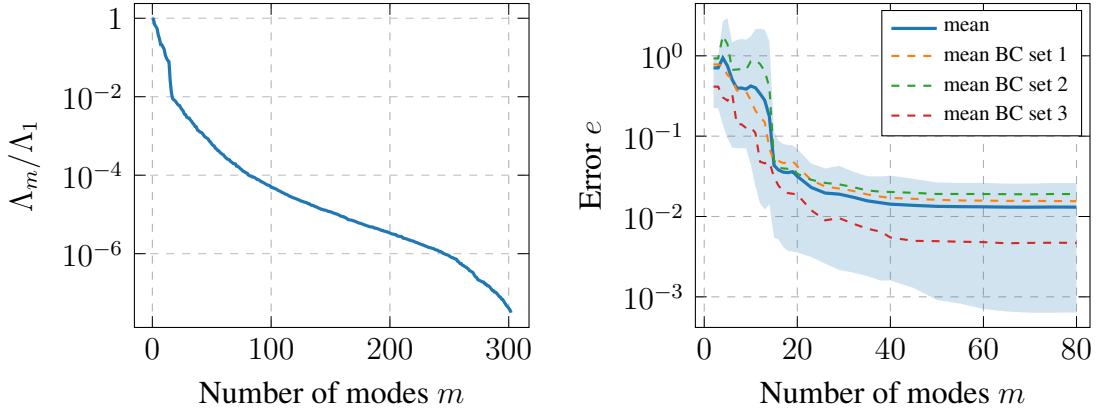


Figure 5: Decay of the normalized singular values (left), and decay of the mean error of ten unseen test samples over the number of modes m . The blue area is the difference between the minimum and maximum mean displacement error.

The test samples show, that the POD basis can approximate the displacement states resulting from the sampling parameter space. In the proposed method the module is used as a substructure of arbitrary systems made of multiple substructures. Since the substructure snapshots are not computed with those systems, the substructure POD basis is non-optimal for some displacement states that could occur in arbitrary systems. These systems can still be approximated if the parameter space mimics possible deformation states of the substructure. A higher number of modes can still increase the accuracy.

3.1.3 Simulation

The accuracy of the substructuring method and substructure modes is evaluated by comparing reduced solutions with full-order mortar tied-contact simulations. In Figure 6 displacement error norms are shown over the applied displacement for different numbers of modes per substructure. In general, the error of the 2×3 structure is higher than that of the 3×3 structure. For all shown number of substructure modes the error is below 1.2%. It can be seen, that by

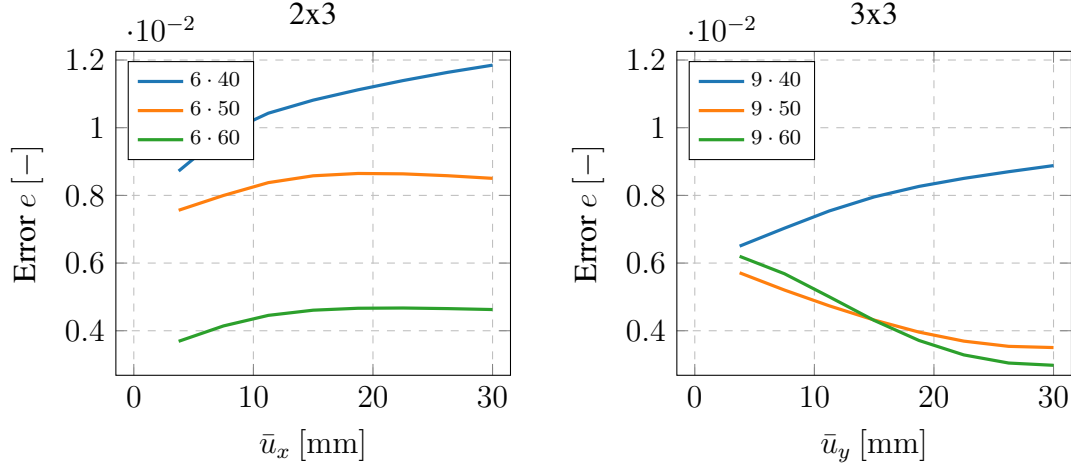


Figure 6: Plot of the displacement error norm over the prescribed displacement for the 2×3 and 3×3 example, for different numbers of substructure modes. For both systems, we show solutions with 40, 50, and 60 modes per substructure.

increasing the number of substructure modes the displacement error decreases. However, for the 3×3 system the displacement error of the simulation with 60 modes per substructure is not in every solution step smaller than the simulation with 50 modes per substructure. For the 2×3 system the error decreases when the number of modes is increased from 50 to 60.

In Figure 7 we show normalized force-displacement diagrams of the two load cases, for an increasing number of substructure modes.

For the system consisting of 2×3 substructures it can be seen that with all three different numbers of modes per substructure, the reference solution can be predicted. For the system with 3×3 substructures, the reaction forces of the reduced solution are overestimated. By increasing the number of modes of the substructure the reaction forces converge to the reference solution. A reason for the overestimation could be that the snapshots are computed with a Young's modulus of $E = 80$ GPa and the softer substructures have a Young's modulus of $E = 20$ GPa.

In Figure 8 and Figure 9 we show the shear stress contour plots as well as the displacements of the two systems. The black outline is the outline of the reference solution computed by the mortar tied-contact method without model order reduction. For the reduced solution of both systems 50 modes per substructure are used. The different displacement states of the substructures in the two systems can all be described by the same substructure modes. The modes can be used to reduce substructures with different numbers of free edges, contact interfaces or interfaces, where boundary conditions are applied. This indicates the versatility of the computed modes.

The reduced order system has approximately 98 times fewer DOFs than the reference model

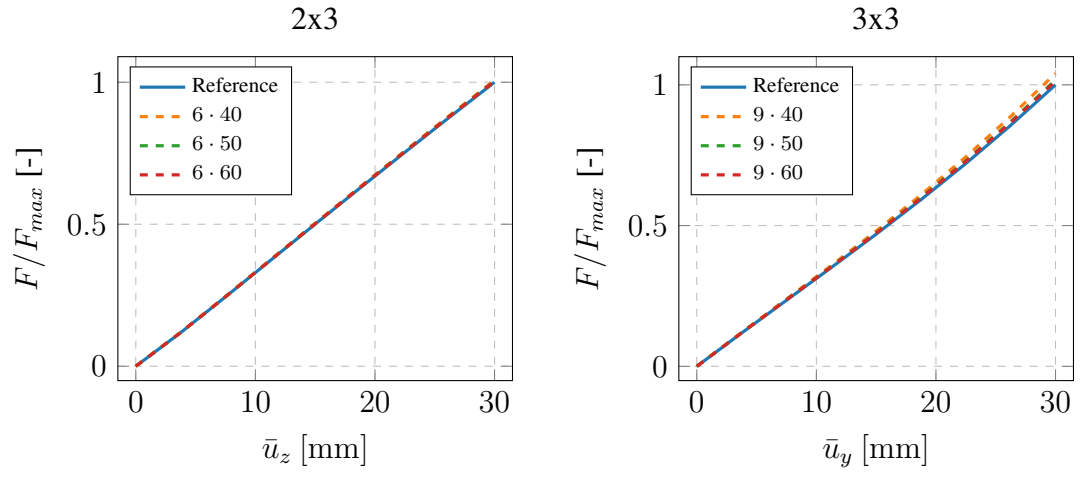


Figure 7: Plot of the reaction forces over the displacements for the 2×3 and 3×3 example. For both systems, we show solutions with 40, 50, and 60 modes per substructure.

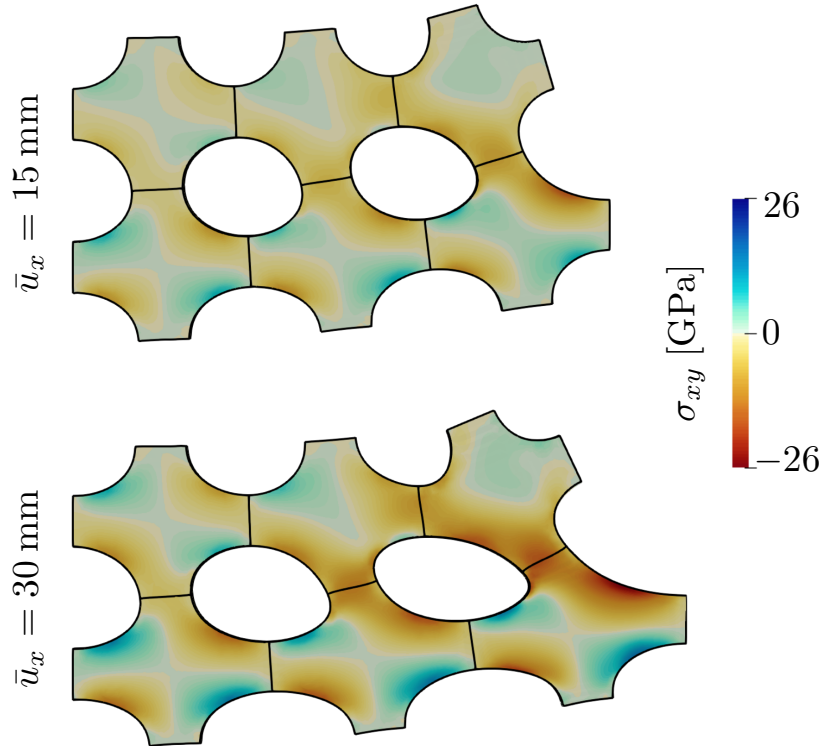


Figure 8: Cauchy shear stress contour plots of the deformed reduced solution. The black outlines are the reference solutions.

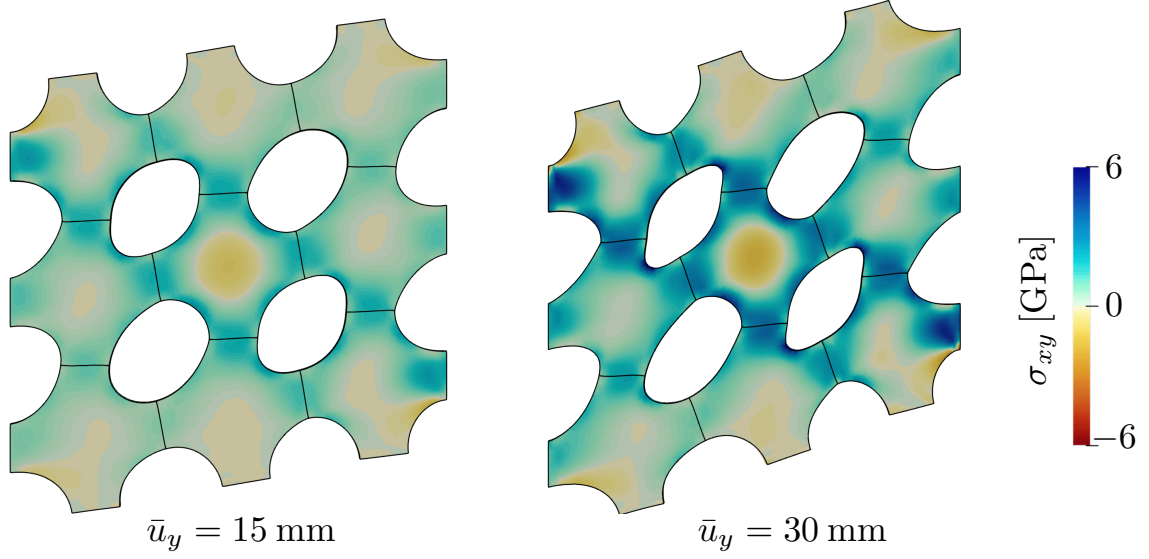


Figure 9: Cauchy shear stress contour plots of the deformed reduced solution. The black outlines are the reference solutions.

$\left(\frac{29358}{300} \approx 98\right)$. The results from Figure 8 show further, that non-matching meshes are possible to solve with the proposed ROM. The system has approximately 82 times fewer DOFs than the reference solution $\left(\frac{36990}{690} \approx 82\right)$. It can also be seen, that the modes computed with the method described in Section 2.3 can be used for different stiffnesses of the substructures.

In Figure 10 we show the yy -component of the Cauchy stress tensor σ at the displayed interface for the ROM and FOM. The black outline indicates the substructure interface. It can be seen that the interface curvature of the ROM is smaller than of the FOM. Consequently, the stresses in the interface region differ. With increasing distance from the interface the stresses are approximated more accurate.

3.2 Example 2: Ring-segment

3.2.1 Boundary value problem

In this numerical example, we use the same substructure in two different systems. The dimensions and mesh of the component are shown in Figure 12. The boundary value problems are illustrated in Figure 11. On the left, four components are assembled into a ring structure, with 15876 DOFs in total. The other system consists of five substructures with 19845 DOFs. The displacement boundary conditions can be seen in Figure 11. In the following, we use the term "ring"-structure for the example on the left and the term "omega" for the structure shown on the right.

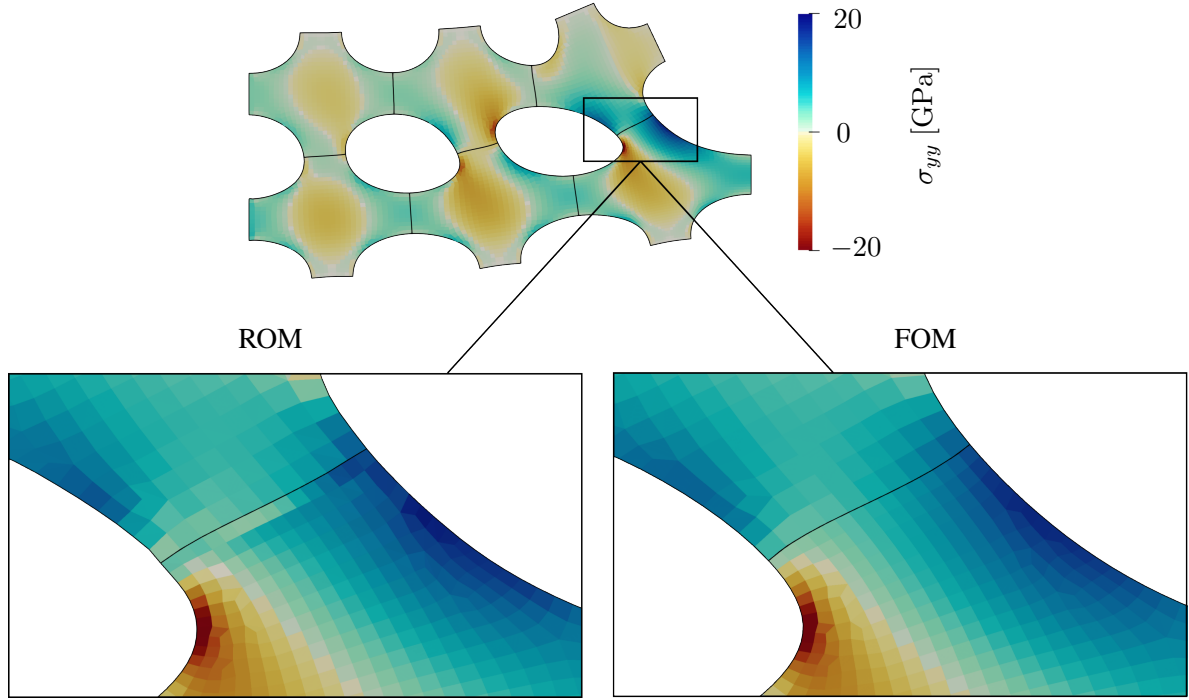


Figure 10: Zoom of the Cauchy stress σ_{yy} contour plots at the interface for the reduced solution (left) and full-order solution (right). The black outlines are the substructure boundaries. The stresses are computed in the center of the element.

In Section 3.2.3 the results for a Neo-Hookean material and in Section 3.2.5 the results for a finite strain viscoelasticity model are shown. For all simulations we use mode matrices computed from the same set of snapshots. The snapshot parametrization is explained in Section 3.2.2.

In Figure 12 we show the meshes of the module used in the numerical examples from Figure 11.

3.2.2 Snapshot computation

The snapshots are computed for the substructure in the middle with the boundary value problem shown in Figure 13. The two substructures, that are attached left and right are used to apply the boundary conditions on the surfaces Γ_u^1 and Γ_u^2 . This makes deflections of the interfaces in x - and y -direction possible. These deflections are necessary, because these interfaces do not remain planar after deformation if the substructures are assembled into larger systems.

On both surfaces, we apply a displacement that depends on six parameters $U_{BC} = U_{BC}(d_x, d_y, d_z, \varphi_x, \varphi_y, \varphi_z)$. The parameters d_x, d_y, d_z describe a displacement of the surface in x, y, z -direction. The parameters $\varphi_x, \varphi_y, \varphi_z$ rotate the surfaces Γ_u^1 and Γ_u^2 around the x, y, z -axes. The

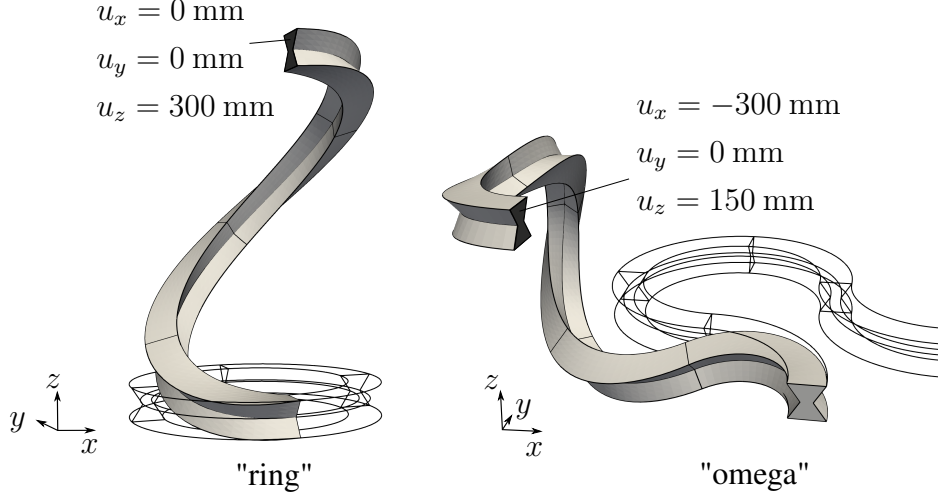


Figure 11: Boundary value problems of two systems "ring" and "omega", that are assembled from the same modules. For both systems, the undeformed configuration is shown as an outline, and the deformed configuration is shown in gray. Both systems are fixed where the deformed and the undeformed configurations coincide. The displacement boundary conditions are applied to the marked area.

parameter ranges for the Latin hypercube sampling (LHS) are:

$$\begin{aligned} d_x &\in (-80, 80) \text{ [mm]} & \varphi_x &\in (-60, 60) [^\circ] \\ d_y &\in (-30, 30) \text{ [mm]} & \varphi_y &\in (-60, 60) [^\circ] \\ d_z &\in (-100, 100) \text{ [mm]} & \varphi_z &\in (-15, 15) [^\circ] \end{aligned}$$

For each random parameter point, we compute two snapshots. One where we apply the displacement to the surface $\Gamma_{\bar{u}}^1$ and set all displacement of the surface $\Gamma_{\bar{u}}^2$ to zero, and a second one where the same displacement is applied to $\Gamma_{\bar{u}}^2$. For the sampling we use a Neo-Hookean material model with the Lamé constants: $\lambda = 14907 \text{ MPa}$, $\mu = 34783 \text{ MPa}$. We compute snapshots at 60 LHS sample points where the displacement boundary condition is applied incrementally in three load steps. Three load steps are necessary to ensure convergence for all parameter combinations. Additionally, we compute snapshots with the minimal and maximal value of each parameter, while all other parameters are zero. This ensures, that the extreme values of the parameter space are covered in the snapshots. Leading in total to a number of 486 snapshots, including also the six rigid body motions.

The POD basis is computed by the singular value decomposition. The decay of the normalized singular values can be seen in Figure 14. Additionally, we generate 10 test samples by Latin hypercube sampling that were not included in the snapshot samples. We analyzed the mean displacement error of these test samples for reduced simulations with increasing number of modes. In the simulations only the substructure in the center is reduced, the pieces at the boundary are unreduced and are used to compute and apply the boundary conditions to the center

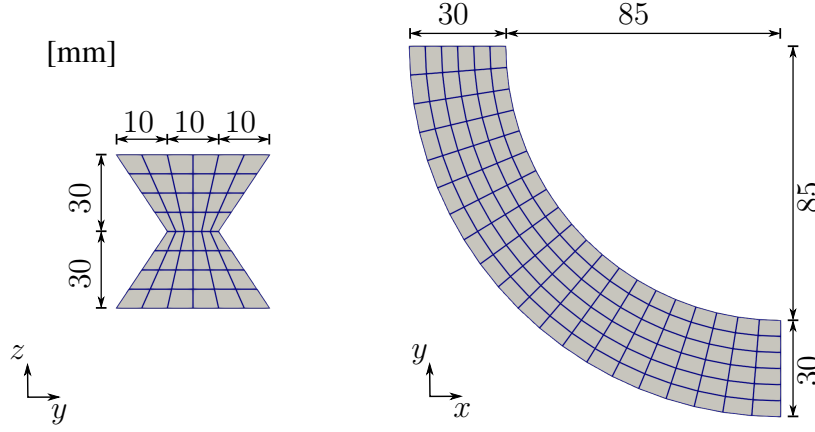


Figure 12: Geometry and mesh of a module. Cross-section (left) and top view (right)

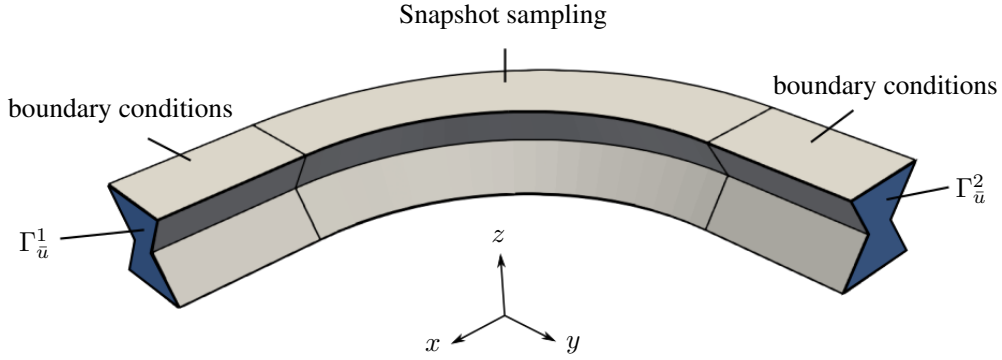


Figure 13: Boundary value problem for the snapshot computation, consisting of three substructures. The snapshots are collected for the central substructure.

substructure.

The mean displacement error e decreases with increasing number of modes. With 40 modes for the ring substructure the maximum error is 1.1%. More modes lead to a further decrease of the error. For 100 modes per substructure the maximum error is 0.2%. In contrast to the displacement error shown in Figure 5 (Section 3.1.2) it does not converge. A difference between those two systems is, that the reduced test sample simulations of the "ring" substructure are computed with the method described in Section 2.2. With the modification, that only the substructure in the center was reduced. The other two substructures were unreduced, because only the POD approximation of the substructure in the center should be tested. It could be possible that the different error behavior is related to this difference.

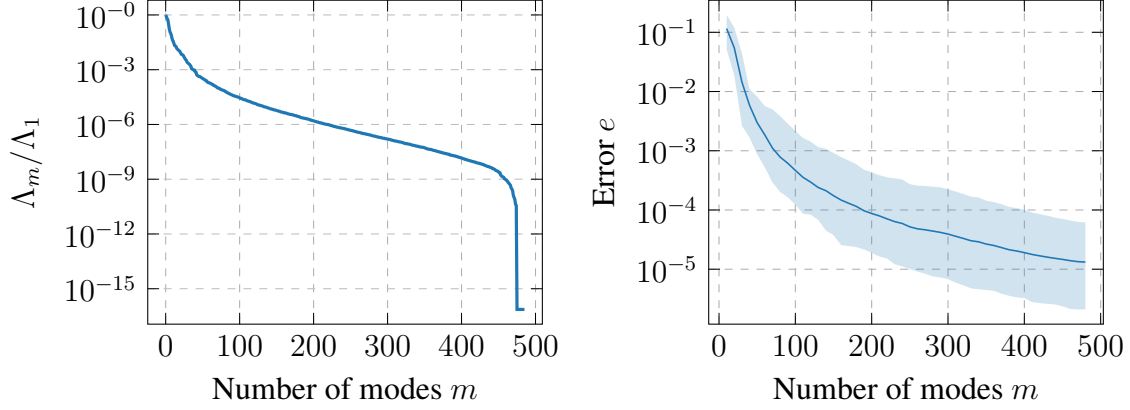


Figure 14: Decay of the normalized singular values (left), and decay of the mean error of ten unseen test samples over the number of modes m . The blue area is the difference between the minimum and maximum mean displacement error.

3.2.3 Neo-Hooke material

First, we investigate the accuracy of the substructuring MOR method and the modes for a Neo-Hookean material. The modes are computed from the snapshots described above in Section 3.2.2. In Figures 23 and 24 in Appendix A.1 we show the deformed structures and the stress contours computed by the here proposed method.

In Figure 15 we compare the accuracy of the displacement field for an increasing number of modes. We also compare the method to the penalty approach proposed in Zhou et al. [2018]. It can be seen, that the proposed method (cf. Section 2.2) is more accurate than the solutions computed by the penalty method. The error norm e for the proposed method is for all three number of modes below 0.15% (the displacement error is defined in Equation (36)). Increasing the number of modes to 80 modes per substructure can reduce the error to 0.05%.

For the penalty method the most accurate results are computed with 60 modes per substructure. Increasing the number of modes here leads to increasing errors. The reason for this behavior is, that the solution depends on the choice of the penalty parameter. If the penalty parameter is too high, the displacements are underestimated. For too small values the reaction forces are overestimated. The accuracy could be increased by choosing a higher penalty parameter. The parameter not only influences the accuracy but also the numerical stability. In this example, the penalty parameter was chosen as $\varepsilon = 10^3$ to get converging results. For this parameter, we needed 10 times more load steps to reach convergence. For higher penalty parameters the reduced solution did not converge at all. The reduced solution underestimates the displacements. If the small penalty parameter overestimates the displacement this can lead to smaller errors even though fewer modes are used.

Similar observations can also be made for the force displacement curves shown in Figure 16.

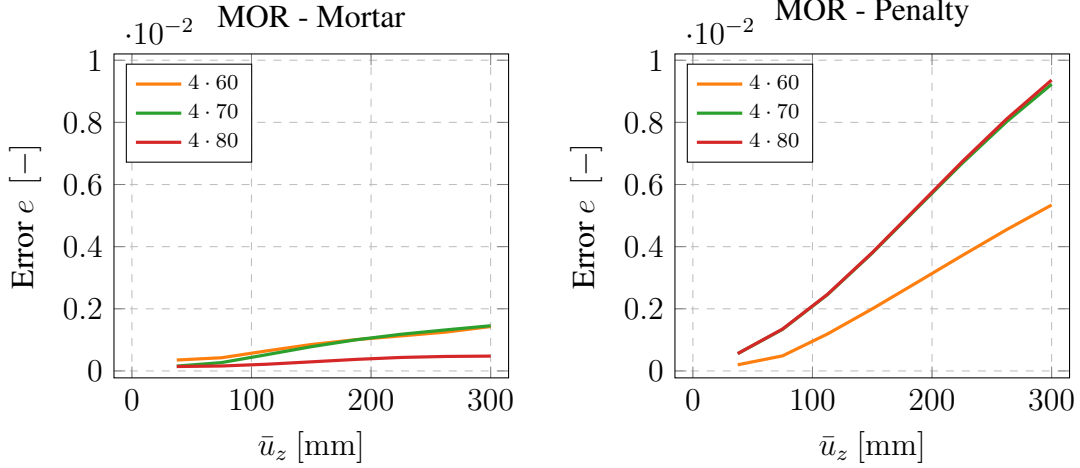


Figure 15: Plot of the displacement error norm over the prescribed displacement of the "ring" example. On the left the contact conditions are enforced by the reduced mortar approach and on the right by the penalty method. For both methods we show solutions with 60, 70, and 80 modes per substructure.

The curves computed by the mortar MOR method converge to the reference solution by increasing the number of modes. For the penalty method the best approximation of the force displacement curve is the simulation with 60 modes per substructure. Increasing the number of modes leads to a underestimation of the reaction forces. The reason is the influence of the penalty parameter on the solution.

Analogously to Figure 15, Figure 17 shows the displacement error norm over the applied total displacement $\sqrt{\bar{u}_x^2 + \bar{u}_z^2}$. The error norms of the mortar method and the penalty method are compared for increasing numbers of modes. Compared to the "ring" example more modes have to be included in order to get accurate results. For 80 modes per substructure the maximum error for the "omega" example is one order of magnitude higher than the error of the "ring" example. Increasing the number of modes can reduce this error. For 120 modes per substructure the maximum error is $e_{\max} = 0.0025$. The penalty solution is less accurate than the mortar solution. For 120 modes per substructure the maximum error is here $e_{\max} = 0.0041$.

In Figure 18 we show the force-displacement curves for the "omega" structure. From the force-displacement curve it can be seen that the system shows stability effects. At a displacement of around $\sqrt{\bar{u}_x^2 + \bar{u}_z^2} \approx 200$ mm the system can deform without increased resistance up to a displacement of $\sqrt{\bar{u}_x^2 + \bar{u}_z^2} \approx 250$ mm, where the reaction forces increase again. The reduced simulation can qualitatively predict this behavior, but the reaction forces are overestimated. The results of the mortar method are closer to the reference solution than the results of the penalty method. For 120 modes per substructure the force error of the mortar method is $(F_{\text{mortar}} - F_{\text{Ref}})/F_{\text{Ref}} = 0.035$. The force error of the penalty method is nearly twice as high with $(F_{\text{penalty}} - F_{\text{Ref}})/F_{\text{Ref}} = 0.068$.

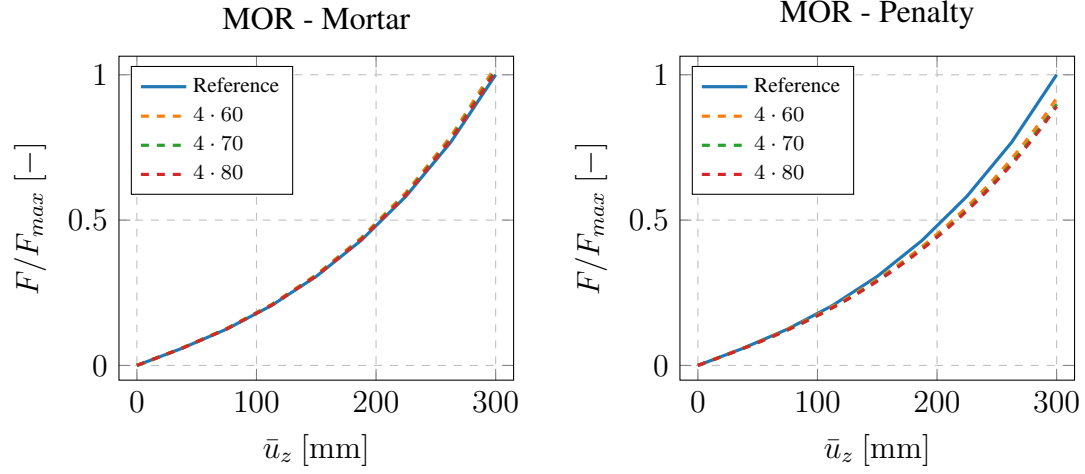


Figure 16: Force displacement curve of the "ring" example for the two different approaches that enforce the tied contact condition. The mortar approach is shown on the left and the penalty approach on the right. For both methods we show solutions with 60, 70, and 80 modes per substructure.

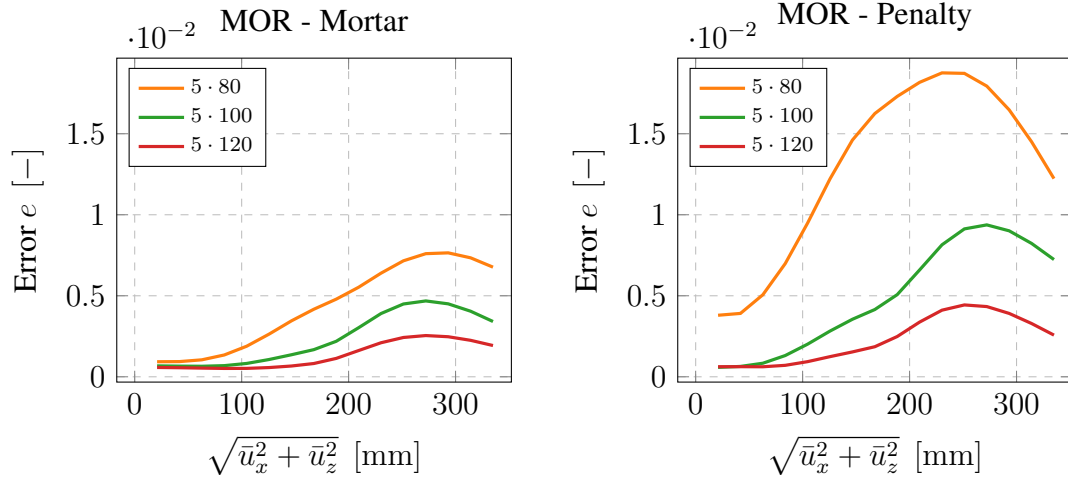


Figure 17: Plot of the displacement error norm over the prescribed displacement of the "omega" example. On the left the contact conditions are enforced by the reduced mortar approach and on the right by the penalty method. For both methods we show solutions with 80, 100, and 120 modes per substructure.

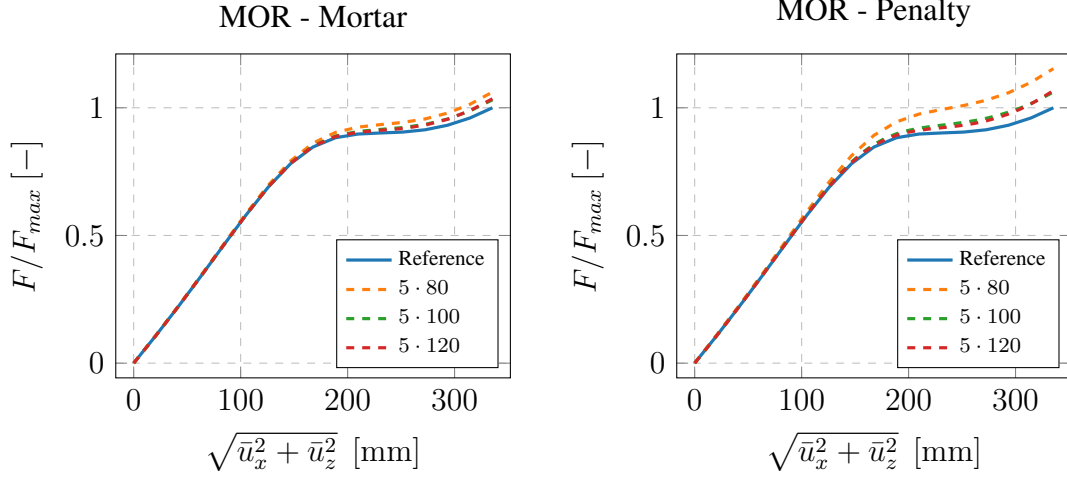


Figure 18: Force displacement curve of the omega-shaped example for the two different approaches that enforce the tied contact condition. The mortar approach is shown on the left and the penalty approach on the right. For both methods we show solutions with 80, 100, and 120 modes per substructure.

In Figure 19 we show the relative simulation times regarding the total simulation time of the FOM. For the "ring" structure the simulation time is 33.12 % of the FOM time and for the "omega" structure it is 37.47 %. In Figure 19 we split the simulation times into two parts. Firstly, the assembly of the system and, secondly, the solution of the system. Most time savings were achieved in the solution of the system since the dimension of the ROM is smaller than the dimension of the FOM. The assembly of the system cannot be sped up by the current reduced model, because in every iteration each element stiffness matrix and residual has to be called and projected into the reduced space. Hyperreduction techniques like ECSW could reduce this computational effort.

3.2.4 Load-parametrization

This numerical example demonstrates the versatility of the modes and snapshots generated by the parametrization described in Section 3.2.2. The geometry and boundary conditions are the same as in the "omega" example. The only difference is that we parametrize the applied displacement in x -direction. The x -displacements vary from $\bar{u}_x = -300$ mm to $\bar{u}_x = 300$ mm. The simulations are computed in increments of 50 mm. The displacement in z -direction is in all cases $\bar{u}_z = 150$ mm. All displacement states are visualized in Figure 20.

Figure 21 shows the displacement error over the applied displacement \bar{u}_x . It can be seen, that for 80 modes per substructure the results are less accurate than the results computed with 100 or 120 modes per substructure. The solution with 120 modes per substructure is only at the ends of the parameter space more accurate than the solution with 100 modes per substructure.

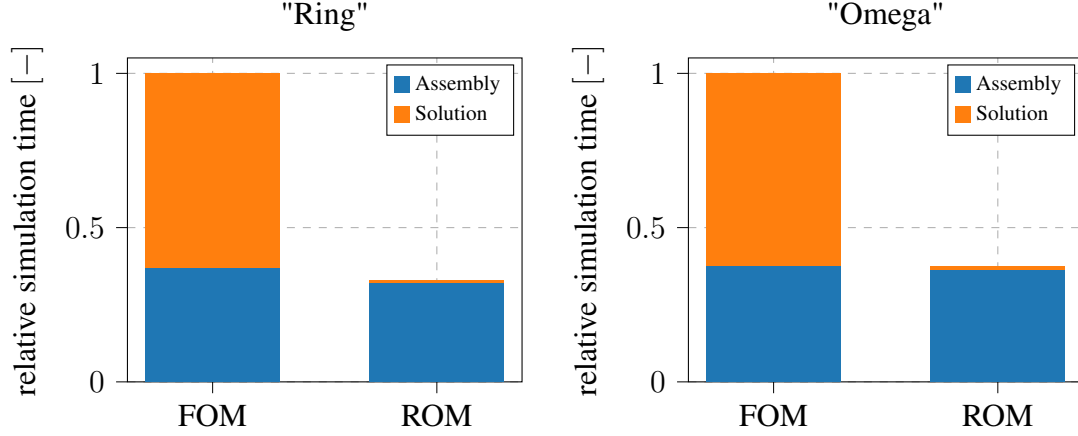


Figure 19: Comparison of the solution time of a timestep, differentiating between the solution steps assembly and solution. Normalized time the full order model (FOM) and the mortar reduced order model (ROM), for the "ring" example (left) and the "omega" example (right).

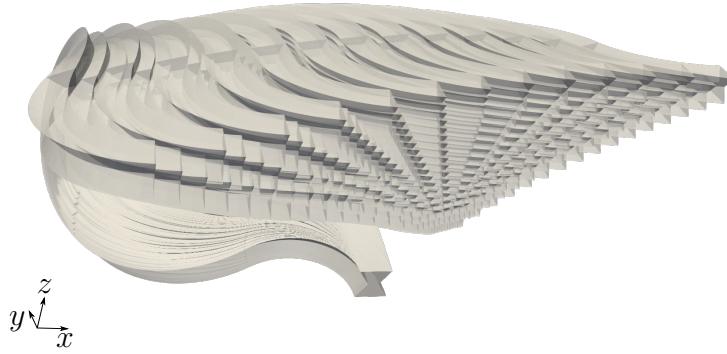


Figure 20: All displacement states of the parametrized "omega" example. The x -displacements vary from $\bar{u}_x = -300$ mm to $\bar{u}_x = 300$ mm. The displacement $\bar{u}_z = 150$ mm is constant.

Between $\bar{u}_x = -100$ mm and $\bar{u}_x = 100$ mm 100 modes per substructure give the most accurate results. A reason could be that the displacement state for this parameter range is better covered by the snapshots. For larger displacements the error can then be reduced by taking more modes into account.

3.2.5 Viscoelasticity

In this section, we show that for inelastic material behavior, we can use the same modes as above. The modes are computed with a Neo-Hookean material (cf. Section 3.2.2) and are used now to reduce finite strain viscoelasticity. We simulated the "omega" boundary value problem now with a viscoelastic material law, according to Reese and Govindjee [1998]; Holthusen et al.

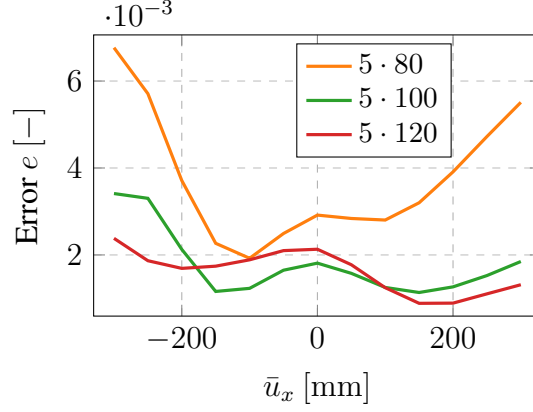


Figure 21: Plot of the displacement error norm over the applied displacement \bar{u}_x for 80, 100, and 120 modes per substructure.

[2023]. The displacement is applied over different time periods. The force-displacement curves in Figure 22 show the rate dependence of the reaction forces. The slower the displacement is applied, the smaller the reaction force.

The reduced computation is computed with 100 modes per substructure. The mode matrix is the same that we also used for the example with a Neo-Hookean material. It can be seen that the nonlinear force-displacement curves can be qualitatively reproduced by the reduced computation. For all three displacement rates the maximum force error is $(F_{\text{MOR}} - F_{\text{Ref}})/F_{\text{Ref}} \approx 0.04 \pm 0.001$. This error is similar to the errors of the elastic simulations Section 3.2.3, where the maximum reaction force error was $(F_{\text{MOR}} - F_{\text{Ref}})/F_{\text{Ref}} = 0.035$. It can be concluded, that the elastic substructure modes can also be used to successfully predict the force response of viscoelastic simulations.

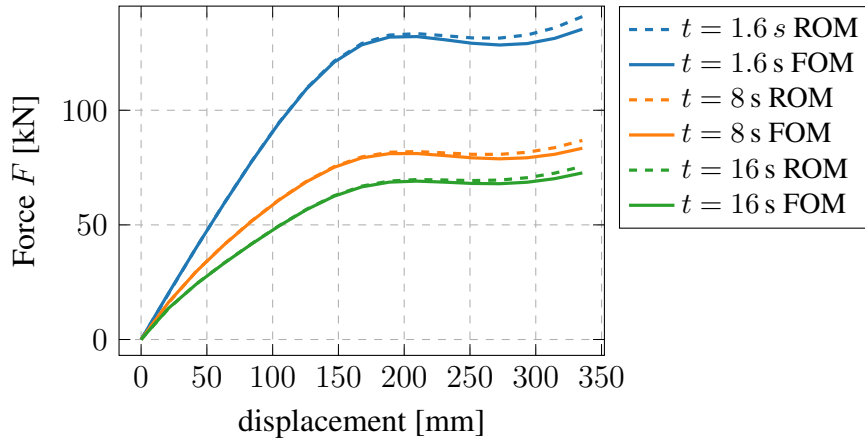


Figure 22: Force-displacement curves for different displacement rates considering finite strain viscoelasticity. The mortar approach is used for the reduced computation, with 100 modes per substructure.

4 Discussion, conclusions and outlook

In this paper, we have developed a substructuring technique using component-wise model order reduction and a mortar tied-contact formulation. In the numerical examples, we demonstrated that the developed method can predict solutions of systems constructed from reduced substructures. The method can handle non-matching meshes, different stiffnesses, geometric nonlinearities and material nonlinearities (finite strain viscoelasticity). The POD modes used for the substructure reduction were computed by simulating the substructures for different boundary conditions. We parametrized the boundary conditions on possible contact interfaces and used Latin hypercube sampling for the snapshot generation.

We also compared the mortar approach, where we removed the Lagrange multipliers by static condensation, to the penalty approach used in Zhou et al. [2018]. The mortar approach has multiple advantages compared to the penalty approach. The penalty approach has convergence problems for the here-discussed numerical examples. It also leads to ill-conditioned tangential stiffness matrices. We presume that the projection of this ill-conditioned tangential stiffness matrix leads to the observed convergence problems. Not for all penalty parameters a solution can be found, and many more load steps are necessary compared to the mortar approach. The solution then also depends on the choice of the penalty parameter. The mortar approach does not have all these issues but has the disadvantage that the implementation is more complicated.

The proposed method requires many modes per substructure to produce accurate results. In future works, local POD methods will be investigated to reduce the size of the POD bases of the substructures (cf. e.g. Amsallem et al. [2012]; Strazzullo and Vicini [2023]).

The here proposed method still depends on the original dimensions of the problem. In the future, we will incorporate hyperreduction methods into the method. Possible methods could be energy conserving sampling and weighting (ECSW) (Farhat et al. [2015]), or the discrete empirical interpolation method (DEIM) (Chaturantabut and Sorensen [2010]). The method can then also be applied to other nonlinear mechanical substructuring problems, e.g. structural dynamics or mechanical meta-materials. In the future, we will also address other material nonlinearities, such as damage and plasticity (e.g. Brepols et al. [2017]; Kehls et al. [2023]).

5 Declaration of competing interest

The authors declare that they have no known competing financial interests or personal relationships that could have appeared to influence the work reported in this paper.

6 Data availability

Data will be made available on request.

7 Acknowledgements

The authors gratefully acknowledge the funding granted by the German Research Foundation (DFG). The results presented here were developed within the subproject A01 of the Transregional Collaborative Research Center (CRC) Transregio (TRR) 280 with project number 417002380. Furthermore, T. Brepols, J. Kehls, and S. Reese gratefully acknowledge the funding that was granted within the subproject B05 "Coupling of intrusive and non-intrusive locally decomposed model order reduction techniques for rapid simulations of road systems" of the DFG CRC/TRR 339 with the project number 453596084, that was strongly involved in the origin of the paper. The authors acknowledge the work of Hagen Holthusen whose element and material implementations were included into the model order reduction finite element program.

8 Funding

German Research Foundation (DFG), project number 417002380

A Appendix

A.1 Stress Contour plots of Example 2

References

- Amsallem, D., Zahr, M. J. and Farhat, C. [2012], ‘Nonlinear model order reduction based on local reduced-order bases’, *International Journal for Numerical Methods in Engineering* **92**(10), 891–916.
- Benner, P., Gugercin, S. and Willcox, K. [2015], ‘A Survey of Projection-Based Model Reduction Methods for Parametric Dynamical Systems’, *SIAM Review* **57**(4), 483–531.
- Benzi, M., Golub, G. H. and Liesen, J. [2005], ‘Numerical solution of saddle point problems’, *Acta numerica* **14**, 1–137.

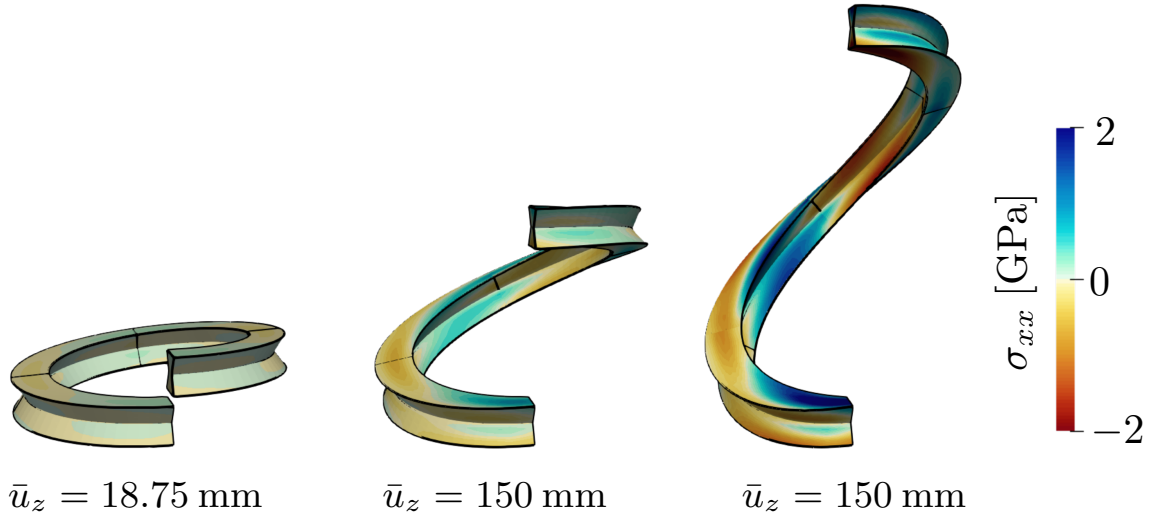


Figure 23: Shear stress contour plots of the deformed reduced solution of the "ring" boundary value problem. The system is solved by the substructuring MOR method with 80 modes per substructure. The black outline is the reference solution.

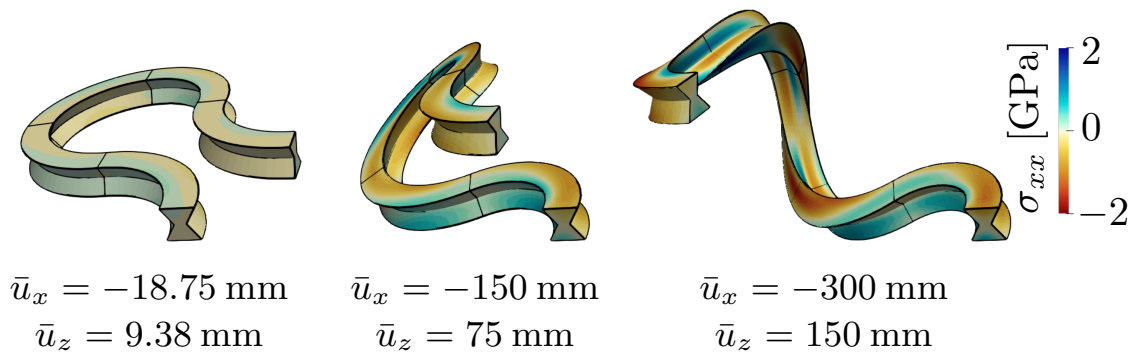


Figure 24: Shear stress contour plots of the deformed reduced solution of the "omega" boundary value problem. The system is solved by the substructuring MOR method with 120 modes per substructure. The black outline is the reference solution.

- Brepols, T., Wulfinghoff, S. and Reese, S. [2017], ‘Gradient-extended two-surface damage-plasticity: micromorphic formulation and numerical aspects’, *International Journal of Plasticity* **97**, 64–106.
- Bui, T. A., Park, J. and Kim, J.-S. [2024], ‘A reduced-order model for geometrically nonlinear curved beam structures with substructuring techniques’, *International Journal of Non-Linear Mechanics* **162**, 104724.
- Bui-Thanh, T., Willcox, K. and Ghattas, O. [2008], ‘Model Reduction for Large-Scale Systems with High-Dimensional Parametric Input Space’, *SIAM Journal on Scientific Computing* **30**(6), 3270–3288. Publisher: Society for Industrial and Applied Mathematics.
- Chaturantabut, S. and Sorensen, D. C. [2010], ‘Nonlinear Model Reduction via Discrete Empirical Interpolation’, *SIAM Journal on Scientific Computing* **32**(5), 2737–2764. Publisher: Society for Industrial and Applied Mathematics.
- Craig, R. R. and Bampton, M. C. C. [1968], ‘Coupling of substructures for dynamic analyses.’, *AIAA Journal* **6**(7), 1313–1319. Publisher: American Institute of Aeronautics and Astronautics.
- de Klerk, D., Rixen, D. J. and Voormeeren, S. N. [2008], ‘General Framework for Dynamic Substructuring: History, Review and Classification of Techniques’, *AIAA Journal* **46**(5), 1169–1181.
- Farhat, C., Chapman, T. and Avery, P. [2015], ‘Structure-preserving, stability, and accuracy properties of the energy-conserving sampling and weighting method for the hyper reduction of nonlinear finite element dynamic models’, *International Journal for Numerical Methods in Engineering* **102**(5), 1077–1110.
- Ghavamian, F., Tiso, P. and Simone, A. [2017], ‘Pod–deim model order reduction for strain-softening viscoplasticity’, *Computer Methods in Applied Mechanics and Engineering* **317**, 458–479.
- Guo, T., Rokoš, O. and Veroy, K. [2024], ‘A reduced order model for geometrically parameterized two-scale simulations of elasto-plastic microstructures under large deformations’, *Computer Methods in Applied Mechanics and Engineering* **418**, 116467.
- Haasdonk, B. and Ohlberger, M. [2008], ‘Reduced basis method for finite volume approximations of parametrized linear evolution equations’, *ESAIM: Mathematical Modelling and Numerical Analysis* **42**(2), 277–302.
- Herkt, S., Dreßler, K. and Pinnau, R. [2009], ‘Model reduction of nonlinear problems in structural mechanics’.

- Hernández, J. A. [2020], ‘A multiscale method for periodic structures using domain decomposition and ECM-hyperreduction’, *Computer Methods in Applied Mechanics and Engineering* **368**, 113192.
- Hernández, J. A., Bravo, J. R. and Ares de Parga, S. [2024], ‘CECM: A continuous empirical cubature method with application to the dimensional hyperreduction of parameterized finite element models’, *Computer Methods in Applied Mechanics and Engineering* **418**, 116552.
- Hernández, J. A., Caicedo, M. A. and Ferrer, A. [2017], ‘Dimensional hyper-reduction of non-linear finite element models via empirical cubature’, *Computer Methods in Applied Mechanics and Engineering* **313**, 687–722.
- Holthusen, H., Rothkranz, C., Lamm, L., Brepols, T. and Reese, S. [2023], ‘Inelastic material formulations based on a co-rotated intermediate configuration—application to bioengineered tissues’, *Journal of the Mechanics and Physics of Solids* **172**, 105174.
- Kehls, J., Kastian, S., Brepols, T. and Reese, S. [2023], ‘Reduced order modeling of structural problems with damage and plasticity’, *PAMM* **23**(4), e202300079.
- Kerschen, G., Golinval, J.-c., VAKAKIS, A. F. and BERGMAN, L. A. [2005], ‘The Method of Proper Orthogonal Decomposition for Dynamical Characterization and Order Reduction of Mechanical Systems: An Overview’, *Nonlinear Dynamics* **41**(1), 147–169.
- Kuether, R. J., Allen, M. S. and Hollkamp, J. J. [2016], ‘Modal Substructuring of Geometrically Nonlinear Finite-Element Models’, *AIAA Journal* **54**(2), 691–702.
- Kuether, R. J., Allen, M. S. and Hollkamp, J. J. [2017], ‘Modal Substructuring of Geometrically Nonlinear Finite Element Models with Interface Reduction’, *AIAA Journal* **55**(5), 1695–1706.
- Laursen, T. A., Puso, M. A. and Sanders, J. [2012], ‘Mortar contact formulations for deformable–deformable contact: Past contributions and new extensions for enriched and embedded interface formulations’, *Computer Methods in Applied Mechanics and Engineering* **205-208**, 3–15.
- Lenaerts, V., Kerschen, G. and Golinval, J.-C. [2001], ‘Proper orthogonal decomposition for model updating of non-linear mechanical systems’, *Mechanical Systems and Signal Processing* **15**(1), 31–43.
- McBane, S., Choi, Y. and Willcox, K. [2022], ‘Stress-constrained topology optimization of lattice-like structures using component-wise reduced order models’, *Computer Methods in Applied Mechanics and Engineering* **400**, 115525.

- Popp, A. and Wriggers, P., eds [2018], *Contact Modeling for Solids and Particles*, Vol. 585 of *CISM International Centre for Mechanical Sciences*, Springer International Publishing, Cham.
- Puso, M. A. [2004], ‘A 3D mortar method for solid mechanics’, *International Journal for Numerical Methods in Engineering* **59**(3), 315–336.
- Radermacher, A. and Reese, S. [2013a], ‘A comparison of projection-based model reduction concepts in the context of nonlinear biomechanics’, *Archive of Applied Mechanics* **83**(8), 1193–1213.
- Radermacher, A. and Reese, S. [2013b], ‘Proper orthogonal decomposition-based model reduction for non-linear biomechanical analysis’, *International Journal of Materials Engineering Innovation* **4**(2), 149.
- Radermacher, A. and Reese, S. [2016], ‘POD-based model reduction with empirical interpolation applied to nonlinear elasticity’, *International Journal for Numerical Methods in Engineering* **107**(6), 477–495. _eprint: <https://onlinelibrary.wiley.com/doi/pdf/10.1002/nme.5177>.
- Reese, S. and Govindjee, S. [1998], ‘A theory of finite viscoelasticity and numerical aspects’, *International Journal of Solids and Structures* **35**(26), 3455–3482.
- Ritzert, S., Macek, D., Simon, J.-W. and Reese, S. [2023], ‘An adaptive model order reduction technique for parameter-dependent modular structures’, *Computational Mechanics*.
- Rusten, T. and Winther, R. [1992], ‘A preconditioned iterative method for saddlepoint problems’, *SIAM Journal on Matrix Analysis and Applications* **13**(3), 887–904.
- Rutzmoser, J. [2018], *Model Order Reduction for Nonlinear Structural Dynamics*, PhD thesis, Technische Universität München.
- Saad, Y. [2003], *Iterative methods for sparse linear systems*, SIAM.
- Scott, L. R. and Zhang, S. [1990], ‘Finite element interpolation of nonsmooth functions satisfying boundary conditions’, *Mathematics of computation* **54**(190), 483–493.
- Strazzullo, M. and Vicini, F. [2023], ‘POD-Based reduced order methods for optimal control problems governed by parametric partial differential equation with varying boundary control’, *Applied Mathematics and Computation* **457**, 128191.
URL: <https://www.sciencedirect.com/science/article/pii/S0096300323003600>
- Wenneker, F. [2013], *Component Mode Synthesis for geometrically nonlinear structures*, PhD thesis, Citeseer.

- Wohlmuth, B. I. [2001], *Discretization Methods and Iterative Solvers Based on Domain Decomposition*, Vol. 17 of *Lecture Notes in Computational Science and Engineering*, Springer Berlin Heidelberg, Berlin, Heidelberg.
- Wulfinghoff, S. [2024], ‘Statistically compatible hyper-reduction for computational homogenization’, *Computer Methods in Applied Mechanics and Engineering* **420**, 116744.
- Zhou, L., Simon, J.-W. and Reese, S. [2018], ‘Proper orthogonal decomposition for substructures in nonlinear finite element analysis: coupling by means of tied contact’, *Archive of Applied Mechanics* **88**(11), 1975–2001.